Negative Coulomb drag between graphene quantum Hall edges

SONG Junwei [1*], GAN Qikang [1*], ZHU Wang [1], WATANABE Kenji [2], TANIGUCHI Takashi [3], YU Geliang [1†], WANG Lei [1,4‡]

1. National Laboratory of Solid-State Microstructures, Collaborative Innovation Center of Advanced Microstructures, School of Physics, Nanjing University, Nanjing 210093, China
2. Research Center for Electronic and Optical Materials, National Institute for Materials Science, Tsukuba 305-0044, Japan
3. Research Center for Materials Nanoarchitectonics, National Institute for Materials Science, Tsukuba 305-0044, Japan
4. Jiangsu Physical Science Research Center, Nanjing 210093, China

Abstract: Coulomb drag refers to the phenomenon in which a current driven through one conducting layer induces a voltage nearby, electrically isolated layer sorely through interlayer Coulomb interactions between charge carriers. It has been extensively studied in various systems, including parallel nanowires, double quantum wells, and double-layer graphene. Here, we report the observation of Coulomb drag in a novel system consisting of two graphene layers separated laterally by a 30 nm gap within the material plane, exhibiting behavior distinct from that in vertical graphene heterostructures. Our experiments reveal pronounced negative drag resistances under an out-of-plane magnetic field at the quantum Hall edges, reaching a maximum when the carrier densities in both graphene layers are tuned to the charge neutrality point via gate voltages. Our work establish two separate and spatially closed quantum Hall edge modes as a new platform to explore electronic interaction physics between one dimensional systems.

Key words: negative Coulomb drag; quantum Hall edges; van der Waals heterostructures

CLC number: O469 **Document code:** A **DOI:** 10.13725/j.cnki.pip.2026.01.001

CONTENTS

I. Introduction 1
II. Emergence of drag signals 2
III. Drag signals in quantum Hall regime 4
IV. Negative lateral Coulomb drag mechanism 5
V. Temperature and current dependence of the drag signal 6
VI. Discussion 8
VII. Methods 9
A. Sample Preparation 9
B. Transport measurement 9
C. SEM imaging 10
Acknowledgments 10
References 10

I. INTRODUCTION

Coulomb interactions are fundamental to a wide range of emergent phenomena in condensed matter systems, particularly in low-dimensional materials, where reduced dimensionality enhances the relative strength of interactions between charge carriers. Coulomb drag measurements serve as an effective means to probe such interactions, as a current driven in one conductor induces a voltage response in a nearby, electrically isolated conductor through interlayer Coulomb coupling. This effect offers direct insights into the nature of carrier correlations in low-dimensional systems[1]. In the presence of a strong perpendicular magnetic field, two-dimensional (2D) electron systems enter the quantum Hall regime, where current is car-

Received date: 2025-11-03
* These authors contributed equally to this work
† E-mail: yugeliang@nju.edu.cn
‡ E-mail: leiwang@nju.edu.cn

ried by one-dimensional (1D) chiral edge channels while the bulk becomes insulating. These quantum Hall edge states provide an ideal platform to investigate nontrivial Coulomb interactions, as Coulomb coupling between spatially separated, closely spaced edges can give rise to momentum and energy transfer without direct tunneling.

Much of the existing work on Coulomb drag focuses on 2D systems, such as graphene[2-9] and semiconductor quantum well structures[10-11]. These studies reveal a variety of intriguing behaviors, including exciton condensation under strong magnetic fields and asymmetric, non-reciprocal drag signals. Such observations indicate the presence of strong interlayer interactions and highlight the potential for exploring correlated electron states in low-dimensional drag systems. In contrast, Coulomb drag in 1D systems has been investigated in parallel quantum wires[12-15], where drag measurements reveal signatures of Wigner crystallization[16-19] and Luttinger liquid[20-21] behavior, phenomena that arise from the strong electron-electron correlations inherent to low-dimensional conductors. More recently, Coulomb drag experiments in mixed-dimensional systems, such as between 1D and 2D conductors[22-24], provide a means to explore how dimensionality influences electron-electron interactions. For example, coupling an InAs nanowire[25] or a single-walled carbon nanotube (1D conductor) with a graphene sheet (2D conductor)[26-27] demonstrates anomalous temperature dependence and nonlinear drag responses. These studies provide valuable insights into the role of dimensionality in modulating electron-electron interactions and offer a promising avenue for further investigation.

In this work, we investigate Coulomb drag between laterally separated, closely spaced graphene regions hosting quantum Hall edge states under high magnetic fields. This lateral configuration enables direct Coulomb coupling between spatially separated edge channels across a nanometric gap, forming a unique 1D-1D interaction geometry within a 2D material. Our experiments reveal pronounced negative drag responses when both edges are tuned to charge neutrality point (CNP, $n = 0$), accompanied by polarity reversal and strong dependence on temperature and drive current. These findings demonstrate inter-edge Coulomb drag in the quantum Hall regime and open a new route to probing correlated edge transport in graphene.

II. EMERGENCE OF DRAG SIGNALS

The schematic illustration of the fabricated device is shown in Figure 1(a), and the optical image of Device A is presented in Figure 1(b). The prepared heterostructure is dry-etched into left and right parts: the top graphite gate (TG), the insulating hexagonal boron nitride (h-BN) layer between the TG and the monolayer graphene, and the monolayer graphene used for measurements are all etched through, whereas the bottom silicon substrate, which serves as the global bottom gate (BG), remains unetched.

During the measurement, one half of the graphene channel is electrically biased and serves as the drive layer, while the other half is used solely to detect the drag signal coupled via Coulomb interactions, thereby functioning as the drag layer. Both graphene regions lie in the same plane. To further characterize this gap, Figure 1(c) presents a false-color high-resolution SEM image of the device, in which the etched break can be clearly identified. The gap is approximately 30 nm wide, and leakage current measurements show that the interlayer leakage remains below 0.1 nA at 10 V. It should be noted that the TG is also etched and separated, which enables independent tuning of the carrier densities in the drive layer and the drag layer.

By tuning the global Si BG voltage, we first characterize the intrinsic longitudinal resistance of the drive-side graphene in Device A at $T = 1.5$ K, defined as $R^{xx}_{\mathrm{drive}} = V^{xx}_{\mathrm{drive}}/I_{\mathrm{drive}}$, as a function of the out-of-plane magnetic field and carrier density $n = \frac{1}{\mathrm{e}}C_{\mathrm{bg}}(V_{\mathrm{bg}} - V_0)$, as shown in Figure 1(d). A clear Landau-fan pattern is observed. In addition to the central resistance peak at CNP, satellite resistance peaks appear symmetrically on both the electron and hole sides. This phenomenon originates from the formation of a moiré superlattice during device fabrication: the monolayer graphene is nearly aligned with one of the h-BN layers, and due to their similar lattice constants, interference effects induce a moiré superlattice, which gives

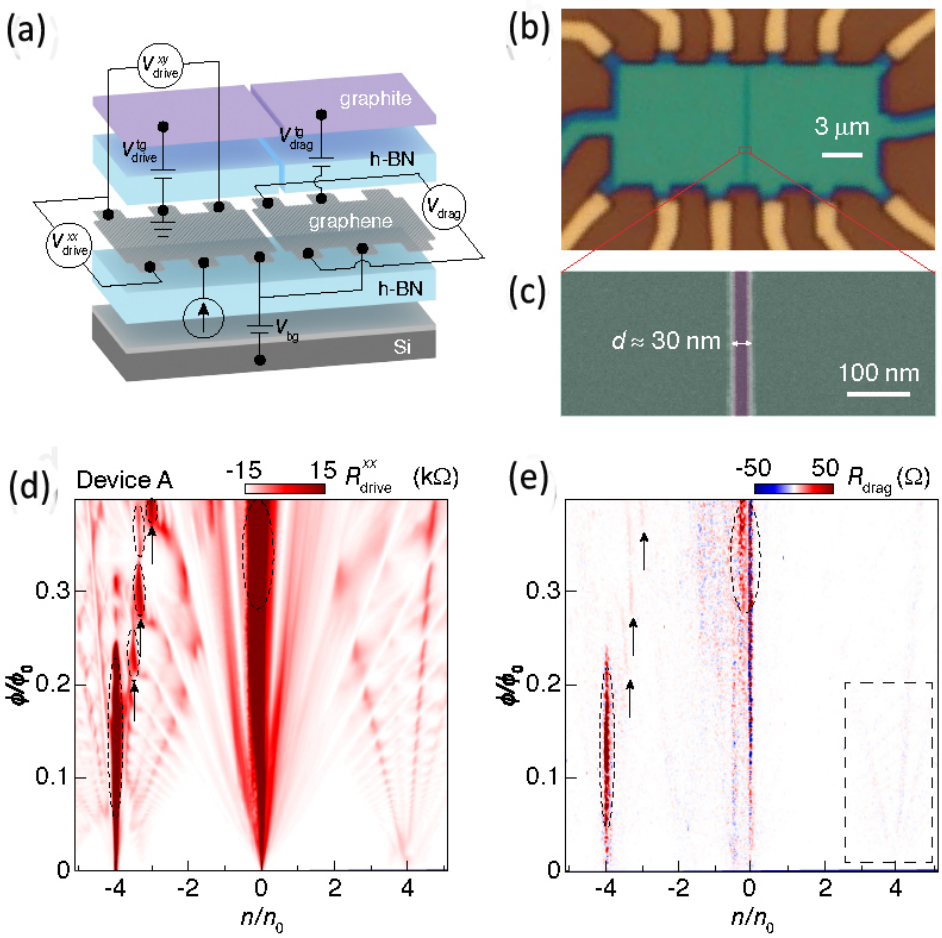


Fig. 1. Coulomb drag in gap-separated graphene. (a) Schematic of the device and measurement setup. The graphene stack is etched into two identical sections, forming the drive and drag layers. The carrier densities in the drive and drag graphene layers are independently controlled via separate graphite TGs and a shared silicon BG. (b) Optical image of Device A. Purple indicates the wafer, green the device, and yellow the metal electrodes. (c) False-color high-resolution scanning electron micrograph showing the detailed structure of the narrow gap (∼30 nm wide). The green area represents the etched stack, and the purple area denotes the etched gap. (d) Landau fan diagram of the longitudinal resistance of the drive layer at $T = 1.5$ K for Device A. The zero-field satellite peak, arising from the graphene/h-BN moiré superlattice, indicates a moiré period of 12.6 nm. (e) Color map of the drag resistance (R_{drag}) as a function of carrier density (n) and magnetic field (B) at $T = 1.5$ K. The axes are normalized to the moiré unit cell.

rise to secondary Dirac points acting as new centers of Landau fans. Moreover, the resistance peaks on the hole side are significantly stronger than those on the electron side, reflecting the intrinsic asymmetry of the moiré potential. Through combined analysis of the periodic interference fringes and the positions of the satellite peaks in the fan diagram, the moiré wavelength is determined to be $\lambda_m = 12.6$ nm. (The horizontal and vertical axes in the figure represent normalized n/n_0 and Φ/Φ_0, corresponding to the electron density and the magnetic flux quanta per unit cell of the superlattice, respectively.)

When simultaneously measuring the longitudinal voltage on the drag side during this process, unconventional voltage signals are detected, as shown in Figure 1(e). The drag resistance, defined as $R_{\mathrm{drag}} = V_{\mathrm{drag}}/I_{\mathrm{drive}}$, exhibits nonzero values in several regions marked by dashed elliptical outlines. Among these, the drag signal corresponding to the satellite peak on the hole side is the most pronounced and stable, reaching a maximum value of approximately 50 Ω. A relatively strong drag signal is also observed at the CNP, though it fluctuates significantly between positive and negative values, indicating lower stability. In addition, at the resistance maxima arising from the interference between the Landau fans centered at the hole-

side satellite peak and the CNP, distinct drag signals of varying amplitudes can also be identified. In contrast, the drag signals on the electron side are much weaker and barely distinguishable in the figure (highlighted by dashed rectangular outlines).

III. DRAG SIGNALS IN QUANTUM HALL REGIME

If Coulomb interactions were absent in the system, the two separated graphene sheets would remain completely electrically independent, and the unbiased graphene layer would not exhibit any electrical signal. However, in our device, the drag layer shows voltage responses consistent with the behavior of the current-driven graphene layer, even though it is not directly biased. This observation provides clear evidence that the drag effect in this device is dominated by Coulomb interactions. Since the two graphene sheets are not vertically stacked but instead separated laterally by an etched 1D gap, the observed drag effect arises from Coulomb forces between carriers across the gap.

It should be noted that the drag signals presented here are extracted from the x-channel (resistive component) of the lock-in amplifier, which ensures the exclusion of any possible contributions from capacitive coupling that would appear in the y-channel (phase-leading component).

We further investigate the Coulomb drag effect under high perpendicular magnetic fields. As shown in Figure 2(a), at $B = 12$ T with the bottom Si BG grounded ($V_{\mathrm{bg}} = 0$ V), we measure a 2D map of R_{drag} as a function of n_{drag} and n_{drive}, which are independently tuned by the TGs of the drag and drive regions, respectively. A pronounced drag signal is observed at $n_{\mathrm{drag}} = 0$, where R_{drag} exceeds 200 Ω.

In addition, a distinct horizontal stripe of enhanced R_{drag} is observed at $n_{\mathrm{drive}} = 0$. Here, R_{drag} also reaches several tens of ohms, although it is significantly weaker than the case of $n_{\mathrm{drag}} = 0$. The underlying mechanism is expected to be analogous to that at the CNP in the drag layer. Moreover, in the second and fourth quadrants, weaker grid-like distributions of high-R_{drag} "islands" can be identified. These states may correspond to resistance maxima induced by the interference between different Landau fans, as previously discussed in Figure 1(e). Finally, a shaded region of suppressed R_{drag} is visible near $n_{\mathrm{drag}} = 0$, which originates from the broadening of the resistance peak at the CNP under high magnetic fields.

However, since R_{drag} is calculated as the ratio of V_{drag} to I_{drive}, and I_{drive} may decrease when the resistance of the drive layer increases, a more direct assessment of the drag effect can be obtained by analyzing V_{drag} alone. As shown in Figure 2(b), the V_{drag} map exhibits a pattern similar to that of Figure 2(a), with strong responses observed at both $n_{\mathrm{drag}} = 0$ and $n_{\mathrm{drive}} = 0$, reaching maxima exceeding 40 μV.

To examine in more detail the effect of tuning n_{drive} on the drag signal, Figure 2(c) presents line cuts of V_{drag} and I_{drive} corresponding to $n_{\mathrm{drag}} = 0$ in Figure 2(b). The V_{drag} signal reaches its maximum (200 μV) at $n_{\mathrm{drive}} = 0$, where I_{drive} simultaneously reaches a minimum due to the zero doping condition in the drive layer. Away from $n_{\mathrm{drive}} = 0$, V_{drag} rapidly decreases as I_{drive} increases. The response is not perfectly symmetric with respect to the sign of n_{drive}: when holes are doped in the drive layer, V_{drag} is larger and I_{drive} is smaller compared to electron doping. Consequently, the overall drag effect is slightly stronger for hole-doped conditions than for electron-doped conditions.

The response of the drag signal to n_{drag} at $n_{\mathrm{drive}} = 0$ shows a different behavior. As shown by the blue curve in Figure 2(d), at $B = 12\,\mathrm{T}$ and $n_{\mathrm{drive}} = 0$, R_{drag} exhibits multiple peaks as n_{drag} is varied. To avoid the influence of the large drag peak at $n_{\mathrm{drag}} = 0$, only the range $0.5 \lesssim n_{\mathrm{drag}}/n_0 \lesssim 3$ is shown. Unlike the monotonic behavior seen in Figure 2(c), here R_{drag} displays several distinct maxima.

To further explore the origin of this feature, we measured the intrinsic Hall signal of the monolayer graphene used on the drive side at $B = 12$ T. As shown by the red curve in Figure 2(d), multiple integer Hall plateaus are observed with increasing n_{drive}, corresponding to filling factors $\nu = 2, 3, 4, 5, 6$. The plateaus at $\nu = 3, 4, 5$ arise from the lifting of spin and valley degeneracies in monolayer graphene under high magnetic fields. Notably, the minima in R_{drag} align with

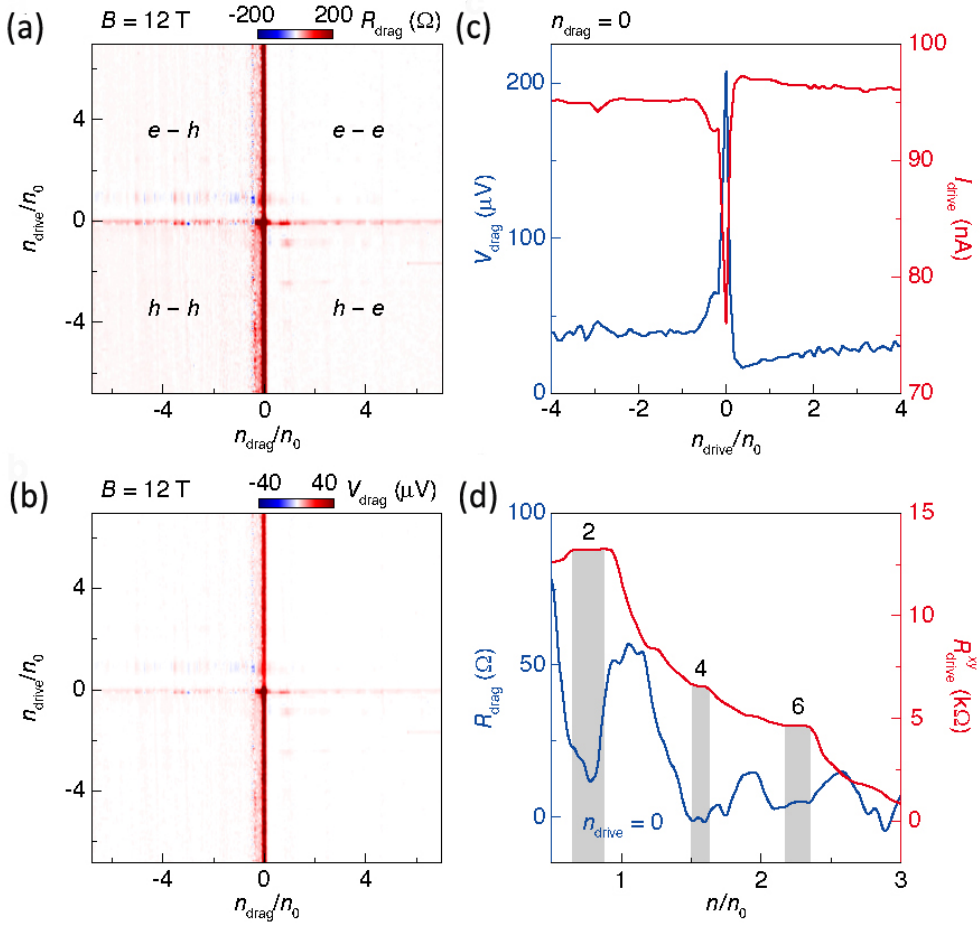


Fig. 2. Coulomb drag measurements at high magnetic field. (a) Drag resistance ($R_{\rm drag}$) at $B = 12$ T and $T = 1.5$ K, shown as a function of the scaled carrier densities of the drag and drive layers. The drag resistance reaches its maximum when both the drive and the drag graphene layers are near the CNP. (b) Corresponding drag voltage for the data shown in (a). (c) Comparison of drag voltage (blue line) and drive current (red line) as functions of the scaled carrier density of the drive layer, with the drag layer held at the CNP. (d) Drag resistance (blue line) as a function of the scaled carrier density of the drag layer, measured away from the CNP while the drive layer is positioned at the CNP. The red line shows the Hall resistance of the drive layer, representing the intrinsic resistive state of the drag layer graphene under equivalent doping conditions.

the even filling factors $\nu = 2, 4, 6$, while the drag signal is larger at $\nu = 3, 5$. One possible explanation is that at $\nu_{\rm drag} = 2, 4, 6$, the bulk is insulating, and the edge states of the drive and drag layers, which mediate the Coulomb drag, do not fully match, resulting in reduced Coulomb coupling efficiency and smaller $R_{\rm drag}$.

IV. NEGATIVE LATERAL COULOMB DRAG MECHANISM

We next perform qualitative measurements of the potential distribution within the device using different measurement configurations. Figures 3(a)∼(d) show 2D maps of $R_{\rm drag}$ as a function of $n_{\rm drag}$ and $n_{\rm drive}$ under four different configurations at $B = 12$ T. The corresponding measurement schematics are illustrated in Figure 3(e), where $V_{1-2} = V_1 - V_2$, and similarly for the other voltage differences.

From Figure 3(a), the drag effect is strongest at locations where R_{1-2} is positive, corresponding to $V_{1-2} > 0$. In Figure 3(b), R_{2-4} is negative, corresponding to $V_{2-4} < 0$, and similarly, Figures 3(c)∼(d) show $V_{3-4} < 0$ and $V_{1-3} > 0$. These observations indicate that points 2 and 3 in Figure 3(e) have lower potentials, whereas points 1 and 4 have higher potentials.

Figure 3(f) illustrates the mechanism underlying this phenomenon. The strong perpendicular magnetic

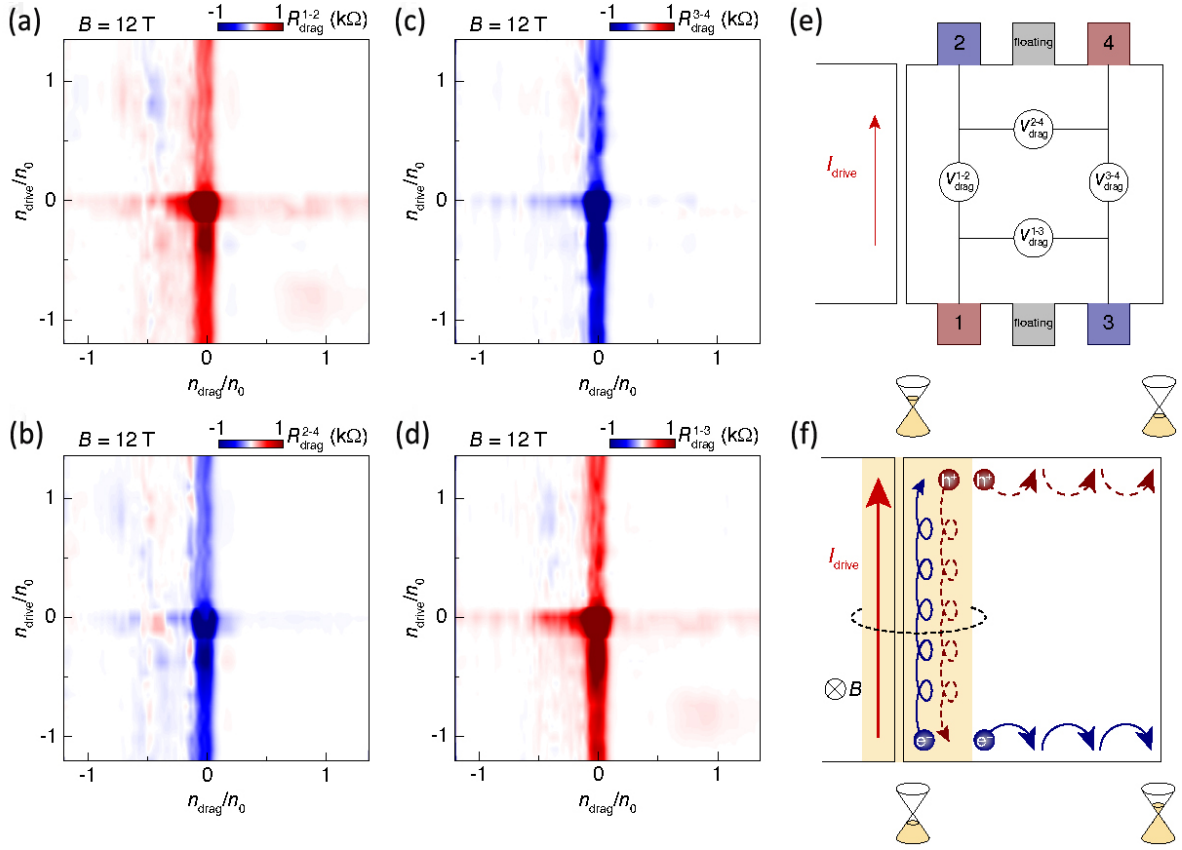


Fig. 3. Various measurement geometries of Coulomb drag. (a)∼(d) Drag resistance ($R^{1-2}_{\rm drag}$ in (a) $R^{2-4}_{\rm drag}$ in (b) $R^{3-4}_{\rm drag}$ in (c) $R^{1-3}_{\rm drag}$ in (d) at $B = 12$ T and $T = 1.5$ K, shown as a function of the scaled carrier densities of the drag and drive layers near the CNP. Electrodes 1 and 4 exhibit higher electric potentials, while electrodes 2 and 3 show lower potentials. (e) Measurement configuration corresponding to (a)∼(d), with all measurements conducted simultaneously. (f) Schematic illustrating the motion of Coulomb-dragged charges within the device.

field forces carriers in the central region of the device into cyclotron motion, preventing them from contributing to conduction. When $I_{\rm drive}$ is applied as shown, the yellow-shaded regions near the edges mark where the Coulomb interaction between the drive and drag layers is strongest, and the electrons and holes there undergo helical motion driven by the combined Lorentz and Coulomb forces. Electrons in the drag layer are Coulomb-dragged upward along the edges, while holes move downward, leading to accumulation of electrons at the upper side and holes at the lower side, which raises the potential at electrode 1 relative to electrode 2. A dynamic equilibrium is established when the Coulomb repulsion generated by the accumulated charges at both sides counterbalances the drag-induced driving force. Meanwhile, some carriers that escape the Coulomb drag process (e.g., holes at the top and electrons at the bottom) move along the device edges as indicated, eventually accumulating and equilibrating at the device ends, forming regions of higher and lower potential corresponding to electrodes 4 and 3, respectively. Similarly, once sufficient charge accumulates near electrodes 3 and 4, the resulting Coulomb potential becomes comparable to the Lorentz force, attracting oppositely charged carriers from the vicinity of electrodes 1 and 2 and partially neutralizing them, leading again to a dynamic equilibrium state.

V. TEMPERATURE AND CURRENT DEPENDENCE OF THE DRAG SIGNAL

In addition to gate tuning, temperature also strongly modulates the drag signal. Figure 4(a) presents the dependence of $R_{\rm drag}$ on the BG voltage $V_{\rm bg}$ and temperature in device B under an out-of-

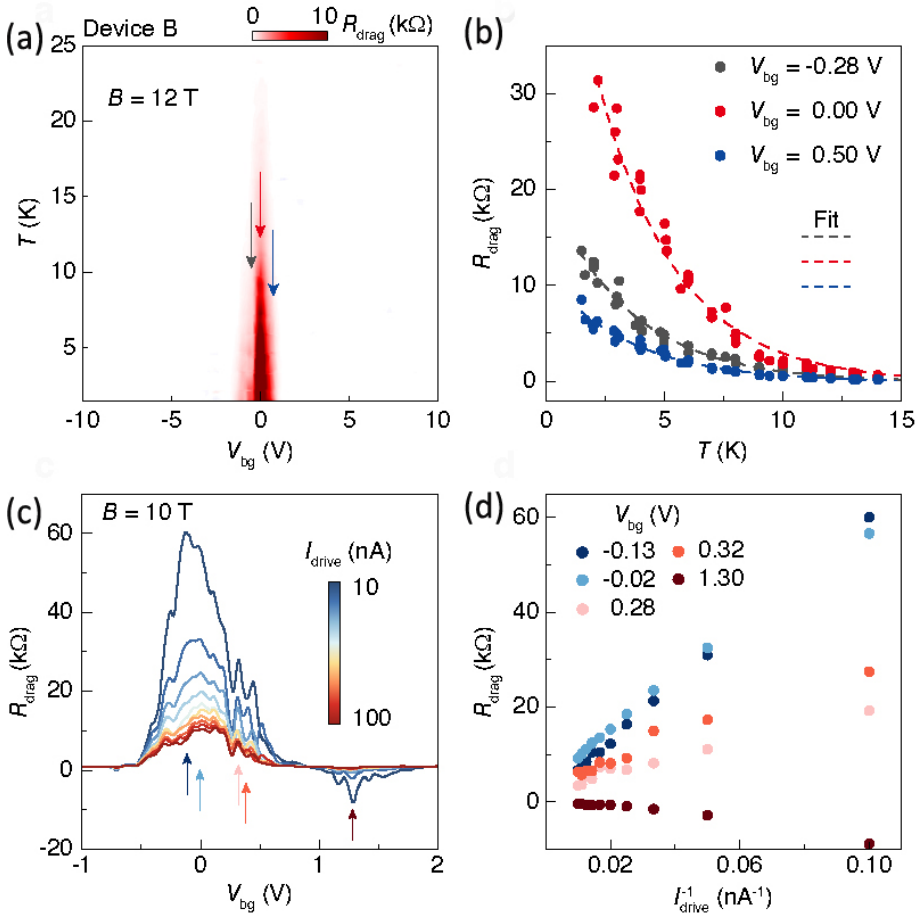


Fig. 4. Influence of temperature and driving current on the drag signa. (a) Map of $R_{\rm drag}$ as a function of BG voltage and temperature at $B = 12$ T and $I_{\rm drive} = 50$ nA for Device B. (b) Temperature dependence of the drag resistance at selected BG voltages, indicated by arrows in (a). The data are well described by $R_{\rm drag} = A \times {\rm e}^{-T/T_0}$, where T_0 represents the characteristic temperature. (c) $R_{\rm drag}$ as a function of BG voltage for different driving currents ($I_{\rm drive}$) at $B = 10$ T. (d) Extracted dependence of $R_{\rm drag}$ on the driving current ($I_{\rm drive}$) for different BG voltages, corresponding to the arrows in (c).

plane magnetic field of $B = 12$ T and a driving current of $I_{\rm drive} = 50$ nA. As the temperature increases, $R_{\rm drag}$ exhibits a pronounced decrease. At $V_{\rm bg} = 0$ V, the drag signal becomes barely distinguishable above $T = 20$ K, while away from the CNP, $R_{\rm drag}$ displays the same decaying behavior with temperature. The extracted $R_{\rm drag}$ as a function of temperature at three representative BG voltages (indicated by arrows in Figure 4(a)) is plotted in Figure 4(b), showing a typical exponential decay. Fitting the data with the function $R_{\rm drag} = A{\rm e}^{-T/T_0}$, where T_0 is defined as the characteristic temperature, yields good agreement between the experimental points and the fitting curves (dashed lines).

Finally, the magnitude of the driving current $I_{\rm drive}$ also modulates $R_{\rm drag}$. Figure 4(c) shows the evolution of $R_{\rm drag}$ as a function of $V_{\rm bg}$ for a series of different driving currents. At smaller currents, the drag resistance becomes larger, and some fine drag peaks become more pronounced. Notably, at $V_{\rm bg} = 1.30$ V, a new negative drag peak emerges when $I_{\rm drive}$ is reduced. By extracting $R_{\rm drag}$ at the BG voltages marked by arrows in Figure 4(c) for different $I_{\rm drive}$, we obtain the data in Figure 4(d), which clearly demonstrate that $R_{\rm drag}$, whether positive or negative, exhibits an inverse proportionality to the driving current.

VI. DISCUSSION

In our study, a pronounced $R_{\rm drag}$ appears at the CNP, whose positive value indicates a negative drag

behavior[16-17]. It is noteworthy that such negative drag at the CNP under magnetic fields has been experimentally observed in 2D drag systems[2-4,6,28].

Several theoretical explanations have been proposed to account for the peak observed at the CNP. One explanation attributes this phenomenon to the third-order interaction terms in the system, which may dominate near the neutrality point[29]. Specifically, at charge neutrality, the unusually strong Coulomb drag in graphene arises from a graphene-specific mechanism based on fast interlayer thermalization rather than conventional momentum transfer. Near the Dirac point, where electron and hole densities are balanced, energy and momentum currents become strongly coupled, allowing efficient transfer of energy fluctuations between the layers even when charge transfer is suppressed. This hydrodynamic regime leads to a finite drag signal that persists in clean samples and, in the presence of disorder or higher-order scattering, produces a pronounced peak in the drag resistivity centered at the neutrality point.

Another explanation considers the peak as originating from interlayer energy transfer mediated by electron-electron interactions[30]. Specifically, at the CNP, the unusually strong Coulomb drag arises from an energy-driven drag mechanism rather than conventional momentum transfer. Because the two graphene layers have spatially correlated electron-hole puddles, a driving current in one layer induces local heating and cooling patterns that are efficiently transferred to the other layer through interlayer electron-electron energy exchange. This correlated temperature modulation generates a thermoelectric voltage in the passive layer, producing a large positive drag peak at neutrality.

In addition, some studies suggest that the strong negative magnetodrag observed at the CNP in graphene may originate from interlayer excitonic correlations analogous to those found in GaAlAs double quantum wells with two half-filled Landau levels[2]. In graphene, the Dirac-like spectrum places the lowest Landau level ($N = 0$) at zero energy, yielding two half-filled levels at the neutrality point that can host electron-hole pairing across layers. Remarkably, such interlayer correlations persist up to room temperature, likely due to the extremely small interlayer spacing relative to the magnetic length, high carrier mobility, and the formation of the $N = 0$ Landau level under finite magnetic fields.

Regarding the observed decrease of R_{drag} with increasing temperature, this may occur in 1D drag configurations where the energy drag mechanism dominates the Coulomb drag, and phonon thermal conductivity plays an important role in weakening the drag signal at elevated temperatures[25]. For the observed reduction of R_{drag} with increasing I_{drive}, possible origins include: (i) a nonlinear drag response in the graphene edge channels, where lower driving currents access the interaction regime dominated by Luttinger liquid physics; (ii) reduced heating effects at small currents, which enhance the relative importance of mesoscopic fluctuations or rectification effects, potentially amplifying or even reversing the drag signal; and (iii) energy transfer or subband filling effects near the CNP, which may also contribute to the emergence of negative drag[30-32].

In conclusion, we clearly observe negative Coulomb drag primarily located at the CNP in laterally separated monolayer graphene under perpendicular magnetic fields. Experiments show that the drag effect exhibits different dependencies on the carrier densities of both the drive and drag layers. Potential measurements further reveal the spatial distribution of the induced voltages, highlighting the role of edge states and cyclotron motion in shaping the drag response. In addition, systematic studies of temperature and current dependence demonstrate that the drag signal decays exponentially with temperature and increases as the drive current is reduced. These results establish lateral graphene heterostructures as a powerful platform to probe Coulomb drag beyond conventional vertically stacked systems.

The results presented here not only expand the understanding of Coulomb drag in graphene but also introduce a novel platform for exploring correlated electronic phases in lateral 2D systems. By combining the advantages of 2D graphene with the spatial separation of layers within the same plane, our findings pave the way for the investigation of new interlayer correlations and quantum condensed states in emerging materials.

VII. METHODS

A. Sample Preparation

The graphene flakes used in the devices originate from mechanical exfoliation of bulk graphite, and the layer number is determined by atomic force microscopy. The multi-layer heterostructures are fabricated using 'pick-up' method[33]. The entire heterostructure assembly is performed on a micromanipulation stage equipped with a temperature-controlled base and a slide clamp fixture. The dry transfer process employs a stamp consisting of a 3 mm-thick Polydimethylsiloxane (PDMS) substrate topped with a poly(propylene carbonate) (PPC) film of several tens of micrometers in thickness as the adhesive layer. A mechanically exfoliated hexagonal boron nitride (h-BN) flake (typically 15∼40 nm thick) is first placed on a heated substrate (maintained at 47 °C throughout the entire transfer process) and then picked up using the transfer stamp. Subsequently, a graphite flake with a thickness of approximately 3∼10 nm is picked up to serve as the TG, followed by the pickup of a thin h-BN flake that functions as the dielectric layer. Next, a monolayer graphene flake is picked up as the device layer, and finally, another h-BN flake is transferred at the bottom of the stack to achieve full encapsulation of the heterostructure. The completed stack is then released onto a heavily doped Si/SiO_2 substrate pre-patterned with alignment marks. After that, a vacuum annealing step (P < 0.01 Pa, 400°C, 35 min) is used to remove the PPC layer.

We first define a ∼300 nm-thick PMMA mask in the shape of a rectangle with electrode leads, depending on the overall size and shape of the material. This is done using electron beam lithography (*ThermoScientific Quattro S*) with an acceleration voltage of 30 kV. The redundant regions of the heterostructure are etched away by CHF_3/O_2 plasma using an *Oxford Instruments PlasmaPro 80 RIE*, which simultaneously exposes the edges of the heterostructure for subsequent edge contacts. After etching, the remaining PMMA mask is removed by rinsing in acetone.

A second round of electron beam lithography is then performed to define the electrode patterns that connect to the pre-designed contact regions. We deposit 5 nm Cr / 15 nm Pd / 60 nm Au electrodes (at a deposition rate of 0.3∼0.8 Å/s) using ultra-high vacuum electron-beam evaporation (*DETECH DE400DUL*), with the chamber pressure maintained below 1×10^{-9} Torr. These edge-contacted electrodes are patterned through a lift-off process by dissolving the PMMA mask in acetone.

A third round of electron beam lithography is performed to cut the graphene and create two adjacent edges. A thinner PMMA mask is prepared by spin coating at a higher speed, and a higher exposure dose is applied to open a narrow window (designed to be ∼20 nm wide) across the heterostructure. The etching is carried out using SF_6/O_2 plasma, and the conductivity across the narrow window is monitored to determine whether the etching is sufficient. Once both the TG and the device-layer graphene are completely cut, the remaining PMMA mask is removed by rinsing in acetone. Finally, the fabricated device is then wire-bonded with Al wires to a dual in-line ceramic chip carrier.

B. Transport measurement

All transport measurements are performed in an *Oxford Instruments TeslatronPT–VS12TMAG* system. During resistance measurements, resistance is measured using a standard four-terminal configuration. A quasi-constant current source is constructed by outputting a 17.777 Hz voltage signal from a *Stanford Research Systems SR830 DSP lock-in amplifier* in series with a 10 MΩ resistor (much larger than all other resistances in the circuit and device). The current is read by a second SR830 lock-in amplifier, synchronized with the source, operating in current mode. The voltage is measured differentially by a third SR830, also synchronized with the source. The TGs on both the drag and drive sides, as well as the Si BG, are independently controlled by three separate *Keithley 2 400* source meters.

When measuring maps, we first fix the parameter corresponding to the y-axis (such as temperature or magnetic field) at its initial value, and then scan the

x-axis variable to acquire data. Once data collection at that y point is complete, we step to the next y value and repeat the process until the full desired range is covered.

C. SEM imaging

The Scanning Electron Microscopy images are captured by an *ThermoScientific Quattro S* with the 30 kV acceleration voltage.

ACKNOWLEDGMENTS

L.W. acknowledges support from the National Key Projects for Research and Development of China (Grant Nos. 2022YFA1204700, 2021YFA1400400), National Natural Science Foundation of China (Grant No. 12525403), Natural Science Foundation of Jiangsu Province (Grant Nos. BK20220066, BK20233001) and Program for Innovative Talents and Entrepreneur in Jiangsu (Grant No.JSSCTD202101). K.W. and T.T. acknowledge support from the JSPS KAKENHI (Grant Numbers 21H05233 and 23H02052) and World Premier International Research Center Initiative (WPI), MEXT, Japan.

REFERENCES

[1] NAROZHNY B, LEVCHENKO A. Coulomb drag[J]. Rev. Mod. Phys., 2016, 88: 025003.

[2] GORBACHEV R, GEIM A K, KATSNELSON M, et al. Strong Coulomb drag and broken symmetry in double-layer graphene[J]. Nat. Phys., 2012, 8: 896.

[3] LEE K Y, XUE J M, DILLEN D C, et al. Giant frictional drag in double bilayer graphene heterostructures[J]. Phys. Rev. Lett., 2016, 117: 046803.

[4] LI J I A, TANIGUCHI T, WATANABE K, et al. Negative Coulomb drag in double bilayer graphene[J]. Phys. Rev. Lett., 2016, 117: 046802.

[5] HU J, WU T, TIAN J, et al. Coulomb drag and counterflow Seebeck coefficient in bilayer-graphene double layers[J]. Nano Energy, 2017, 40: 42.

[6] LIU X M, WANG L, FONG K C, et al. Frictional magneto-Coulomb drag in graphene double-layer heterostructures[J]. Phys. Rev. Lett., 2017, 119: 056802.

[7] LIU X M, WATANABE K, TANIGUCHI T, et al. Quantum Hall drag of exciton condensate in graphene[J]. Nat. Phys., 2017, 13: 746.

[8] ZHU L J, LI L, TAO R, et al. Frictional drag effect between massless and massive fermions in single-layer/bilayer graphene heterostructures[J]. Nano Lett., 2020, 20: 1396.

[9] ZHU L J, LIU X Q, LI L, et al. Signature of quantum interference effect in inter-layer Coulomb drag in graphene-based electronic double-layer systems[J]. Nat. Commun., 2023, 14: 1465.

[10] GAMUCCI A, SPIRITO D, CARREGA M, et al. Anomalous low-temperature Coulomb drag in graphene-GaAs heterostructures[J]. Nat. Commun., 2014, 5: 5824.

[11] SIMONET P, HENNEL S, OVERWEG H, et al. Anomalous Coulomb drag between bilayer graphene and a GaAs electron gas[J]. New J. Phys., 2017, 19: 103042.

[12] RAICHEV O, VASILOPOULOS P. Effects of Coulomb interaction and tunneling on electron transport in coupled one-dimensional systems: from the ballistic to the diffusive regime[J]. Phys. Rev. Lett., 1999, 83: 3697.

[13] RAICHEV O, VASILOPOULOS P. Coulomb drag between parallel ballistic quantum wires[J]. Phys. Rev. B, 2000, 61: 7511.

[14] LEVCHENKO A, KAMENEV A. Coulomb drag in quantum circuits[J]. Phys. Rev. Lett., 2008, 101: 216806.

[15] MAKAJU R, KASSAR H, DALOGLU S M, et al. Nonreciprocal Coulomb drag between quantum wires in the quasi-one-dimensional regime[J]. Phys. Rev. B, 2024, 109: 085101.

[16] YAMAMOTO M, STOPA M, TOKURA Y, et al. Coulomb drag between quantum wires: magnetic field effects and negative anomaly[J]. Physica E, 2002, 12: 726.

[17] YAMAMOTO M, STOPA M, TOKURA Y, et al. Negative Coulomb drag in a one dimensional wire[J]. Science, 2006, 313: 204.

[18] YAMAMOTO M, TAKAGI H, STOPA M, TARUCHA S. Hydrodynamic rectified drag current in a quantum wire induced by wigner crystallization[J]. Phys. Rev. B, 2012, 85: 041308.

[19] LAROCHE D, GERVAIS G, LILLY M, RENO J, Positive and negative Coulomb drag in vertically integrated one dimensional quantum wires[J]. Nat. Nanotechnol. 2011, 6: 793.

[20] LAROCHE D, BIELEJEC E, RENO J, et al. Towards Coulomb drag in vertically coupled quantum wires with independent contacts[J]. Physica E, 2008, 40: 1569.

[21] LAROCHE D, GERVAIS G, LILLY M, RENO J. 1D-1d Coulomb drag signature of a luttinger liquid[J]. Science, 2014, 343: 631.

[22] SIRENKO Y M, VASILOPOULOS P. Influence of dimensionality and statistics on the Coulomb coupling between electron gases or electron-and-hole gases[J]. Phys. Rev. B, 1992, 46: 1611.

[23] LYO S. Coulomb drag between two-dimensional and one-dimensional electron gases[J]. Phys. Rev. B, 2003: 68, 045310.

[24] DEBRAY P, ZVEREV V, RAICHEV O, et al. Experimental studies of Coulomb drag between ballistic quantum wires[J]. J. Phys.: Conden. Matt. 2001, 13: 3389.

[25] MITRA R, SAHU M R, WATANABE K, et al. Anomalous Coulomb drag between inas nanowire and graphene heterostructures[J]. Phys. Rev. Lett., 2020, 124: 116803.

[26] BADALYAN S, JAUHO A P. Coulomb drag between a carbon nanotube and monolayer graphene[J]. Phys. Rev. Res., 2020, 2: 013086.

[27] ANDERSON L, CHENG A, TANIGUCHI T, et al. Coulomb drag between a carbon nanotube and monolayer graphene[J]. Phys. Rev. Lett., 2021, 127: 257701.

[28] TITOV M, GORBACHEV R, NAROZHNY B, et al. Giantmagnetodrag in graphene at charge neutrality[J]. Phys. Rev. Lett., 2013, 111: 166601.

[29] SCHÜTT M, OSTROVSKY P, TITOV M, et al. Coulomb drag in graphene near the dirac point[J]. Phys. Rev. Lett., 2013: 110, 026601.

[30] SONG J C, LEVITOV L S. Energy-driven drag at charge neutrality in graphene[J]. Phys. Rev. Lett., 2012, 109: 236602.

[31] ZHENG M Y, MAKAJU R, GAZIZULIN R, et al. Tunable reciprocal and nonreciprocal contributions to 1D Coulomb drag[J]. Nat. Commun., 2025, 16: 6963.

[32] ZHENG M Y, MAKAJU R, GAZIZULIN R,et al. Quasi-1d Coulomb dragin the nonlinear regime[J]. Phys. Rev. Lett., 2025, 134: 236301.

[33] WANG L, MERIC I, HUANG P Y, et al. One-dimensional electrical contact to a two dimensional material[J]. Science, 2013, 342: 614.

石墨烯量子霍尔边缘间的负库仑拖拽

宋珺威 [1*]，甘祺康 [1*]，朱　旺 [1]，渡边贤司 [2]，谷口尚 [3]，于葛亮 [1†]，王　雷 [1,4‡]

1. 南京大学物理学院，固体微结构物理国家重点实验室，人工微结构科学与技术协同创新中心，南京 210093
2. 日本国立物质材料科学研究所，电子与光功能材料研究中心，筑波 305-0044，日本
3. 日本国立物质材料科学研究所，材料纳米建筑学研究中心，筑波 305-0044，日本
4. 江苏省物理科学研究院，南京 210093

摘要：库仑拖曳是指当电流通过一层导电层时，会在邻近且电学隔离的另一层中产生电压，这一效应完全由载流子之间的层间库仑相互作用引起。该现象已在多种体系中得到广泛研究，包括平行纳米线、双量子阱以及双层石墨烯。在本工作中，我们报道了一种新型体系中库仑拖曳的观测结果，该体系由两层石墨烯组成，层间在同一平面内横向分隔 30 nm，表现出与垂直石墨烯异质结构不同的行为。实验结果显示，在施加垂直磁场时可在相邻的石墨烯边缘处出现明显的负拖曳电阻，当通过栅压将两层石墨烯的载流子浓度调至电荷中性点时，负拖曳达到最大值。本工作建立了一个分立且空间上邻近的量子霍尔边缘系统，为探索一维体系间的电子相互作用物理提供了新的实验平台。

关键词：负库仑拖拽；量子霍尔边缘；范德瓦耳斯异质结

* 共同第一作者

† E-mail: yugeliang@nju.edu.cn
‡ E-mail: leiwang@nju.edu.cn